Multiplexed quantum repeaters based on dual-species trapped-ion systems

Prajit Dhara[1], Norbert M. Linke[2], Edo Waks[3], Saikat Guha[1], and Kaushik P. Seshadreesan[1]*
[1] *Wyant College of Optical Sciences, University of Arizona, Tucson, AZ 85721, USA*
[2] *Joint Quantum Institute and Department of Physics, University of Maryland, College Park, MD 20742, USA and*
[3] *Joint Quantum Institute and Department of Electrical and Computer Engineering, University of Maryland, College Park, MD 20742, USA*
(Dated: May 17, 2021)

Trapped ions form an advanced technology platform for quantum information processing with long qubit coherence times, high-fidelity quantum logic gates, optically active qubits, and a potential to scale up in size while preserving a high level of connectivity between qubits. These traits make them attractive not only for quantum computing, but also for quantum networking. Dedicated, special-purpose trapped-ion processors in conjunction with suitable interconnecting hardware can be used to form quantum repeaters that enable high-rate quantum communications between distant trapped-ion quantum computers in a network. In this regard, hybrid traps with two distinct species of ions, where one ion species can generate ion-photon entanglement that is useful for optically interfacing with the network and the other has long memory lifetimes, useful for qubit storage, has been previously proposed for the distribution of quantum entanglement over the network. We consider an architecture for a repeater based on such a dual-species trapped-ion systems. We propose protocols based on spatial and temporal mode multiplexing for entanglement distribution across a line network of such repeaters. Our protocols offer enhanced performance over previously analyzed protocols for such repeaters.

I. INTRODUCTION

Quantum information processing is set to revolutionize computation, communication and sensing technologies [1, 2]. Applications of these technologies range from quantum speedups with NISQ processors [3] to quantum key distribution [4], to quantum-enhanced distributed sensors [5]. Quantum technologies are currently being actively developed across different physical platforms—from solid-state systems such as superconducting circuits [6] and nitrogen vacancies [7] in diamond, to trapped ions [8], to nano-photonic systems [9]. Quantum networks capable of faithfully transferring quantum states between nodes, including the capability to distribute quantum entanglement [10], are being developed both over short distances to scale up quantum computers in a modular fashion, as well as over long-distances to connect remote quantum computers, or a local area network of computers across physical platforms towards building a global quantum internet [11–13].

Given that photons are the best transmitters of quantum information that can be used to implement scalable quantum communications, the primary challenge in quantum networking is the fundamental rate-loss tradeoff. This trade-off exists for quantum communications over a lossy optical communication channel that models imperfections such as photon collection, coupling and detection inefficiencies, as well as transmission losses. The entanglement distribution capacity of the pure-loss optical channel with unlimited signal power and unlimited local quantum operations and classical communications (LOCC) is given by $C(\eta) = -\log_2(1-\eta)$ ebits per channel-use [14], where η is the channel transmissivity, and an ebit denotes a pair of maximally entangled qubits. In the limit of low transmissivity $\eta \ll 1$, this quantity scales as $\propto \eta$ [15]. As a result, in long-distance communications, say, over an optical fiber link whose transmissivity decreases exponentially with distance as $e^{-\alpha l}$, (α being the fiber loss coefficient per unit length), the entanglement distribution capacity also drops exponentially with distance independent of the presence or absence of other imperfections. Quantum repeaters [16, 17] help overcome this challenge. They are special-purpose quantum computers typically consisting of quantum sources, detectors, elementary logic gates and quantum memories. Quantum repeater architectures based on different physical platforms [18–23] along successive generations of improved protocols [24, 25] have been proposed that can achieve enhanced entanglement distribution rates beyond the direct transmission capacity.

Establishing large-scale quantum links typically calls for setting up a long-distance backbone network. Among the large variety of physical systems that can be utilized to realize quantum repeaters in the backbone quantum network, trapped-ion based systems form an excellent, robust choice, due to their inherently long memory coherence times [26]. Moreover, trapped-ions are known to be an advanced qubit technology [8], and one of the front runners in the race for scalable universal quantum information processing [27]. Repeater networks consisting of single-species trapped-ion nodes have be considered and analyzed in-depth in Ref. [28]. More recently, Santra et al. [29] analyzed repeaters based on ion traps consisting

* kaushiksesh@email.arizona.edu

of two species of ions with complementary properties—a *communication ion* species with good optical properties that enables the network nodes to communicate with each other, and a *memory ion* species having a long coherence time, and therefore suitable for information storage and efficient local quantum processing. Examples of such complementary pairs of ion species include $^{138}\mathrm{Ba}^+$ and $^{171}\mathrm{Yb}^+$, and $^{9}\mathrm{Be}^+$ and $^{25}\mathrm{Mg}^+$. In the former, e.g., the $^{138}\mathrm{Ba}^+$ ion can emit a photon in the visible part of the spectrum (493 nm) that is entangled with the atomic state of the ion. Entanglement can be heralded between the atomic states of two such $^{138}\mathrm{Ba}^+$ ions by performing an optical Bell-state measurement [30] on the photons they emit. Such optically-mediated entanglement, when heralded between adjacent repeater nodes, can be faithfully transferred on to $^{171}\mathrm{Yb}^+$ ions present at the respective nodes, whose atomic states have extremely long coherence times, thus allowing the storage of entanglement between the nodes which can later be processed using efficient quantum gate operations [31, 32]. Santra et al. [29] presented a general repeater architecture based on such dual-species trapped ion (DSTI) modules, and discussed the required set of logic gates to implement repeater protocols. They analyzed the quantum communication rates that can be attained over such a network with specific, simple repeater protocols for the case where each repeater node consists of a single DSTI module. The rates were shown to exceed those possible with direct transmission, and their dependence on experimental parameters were determined.

In the present article, we explore a more general class of repeater protocols based on spatial and temporal multiplexing for the trapped-ion network architecture involving DSTI modules. The spatial multiplexing considered is the same as what was considered in Ref. [29]. Multiple communication ions attempt to generate remote entanglement between every pair of adjacent repeater nodes at each time step of a well-defined clock cycle. In time multiplexing, remote entanglement is heralded from entanglement generation attempts across a block of multiple time steps. With regard to time multiplexing, Ref. [29] considered a fixed clock cycle duration for the photon-ion entanglement generation at the repeater nodes that was determined by the distance between adjacent nodes. On the other hand, we treat the clock cycle duration as a free parameter, where ion-photon entanglement generation at the nodes can be potentially attempted at high rates independent of the inter-node spacing, with a suitably larger number of communication ions and a duly larger number of memory ions to store unheralded ion qubits in the nodes. The corresponding numerically optimal rates are higher than the rates supported by the protocols of Ref. [29]. We identify the number of communication and memory ions necessary to support these new, enhanced rates and discuss the possibility of meeting these requirements with multiple DSTI modules at the repeater nodes.

The article is organized as follows. In Sec. II, we present a general architecture for the trapped-ion repeaters, along with the node operations and an associated error model. In Sec. III, we outline the concepts of spatial and time multiplexing-based quantum repeaters. Section IV contains our proposed protocols based on spatial and time multiplexing for trapped-ion repeaters with two species of ions, along with results for repeaters consisting of $^{138}\mathrm{Ba}^+$ and $^{171}\mathrm{Yb}^+$ ions. We conclude with a discussion and summary in Sec. V.

II. TRAPPED-ION REPEATER ARCHITECTURE

The general architecture for the trapped-ion repeaters and the overall network analyzed in this work is depicted in Fig. 1. The nodes consist of multiple DSTI modules in general, where each module has multiple $^{138}\mathrm{Ba}^+$ ions (which serve as the communication ions) and $^{171}\mathrm{Yb}^+$ ions (which serve as the memory ions), lasers and light collection apparatus, fiber couplers, and optical fibers that connect the DSTI modules to a device such as a quantum reconfigurable add-drop multiplexer (QROADM) [33, 34] whose functionalities include a) frequency conversion to telecom wavelength for inter-node transmissions [35, 36], b) optical switching, and c) linear optical Bell-state measurements. The nodes in the network share a common clock reference. It is assumed that the two species of ions can be excited independently, but only globally, precluding individual ion excitations and readouts. However, it is still assumed that the communication ions are well spaced out so that resonant reabsorption of emitted photons is low, and that light collection is spatially resolved so that spatial multiplexing can be supported. Further, the repeater nodes are assumed to be connected by fiber bundles capable of transmitting multiple single photons in distinct spatial modes.

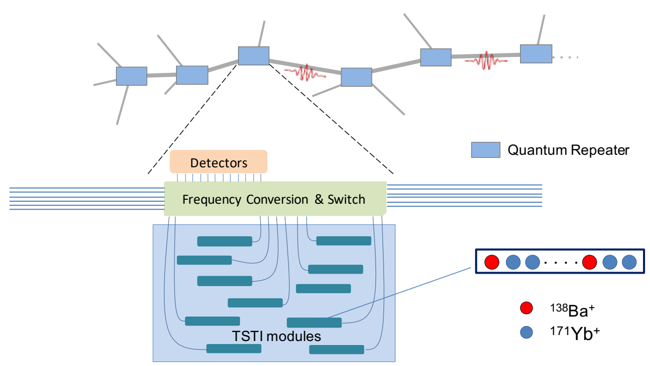

Figure 1. General architecture of a repeater node based on dual-species trapped ion (DSTI) modules to support entanglement distribution protocols based on mode multiplexing. The lines denote optical fibers.

Repeater operations: The basic repeater operations between and at the DSTI modules that we consider were proposed in Santra et al. [29], and are summarized below. Interactions between DSTI modules, both within a repeater node as well as between adjacent repeater nodes are optically mediated. Photons emitted by the communication ions are duly collected, coupled into optical fiber, and interfered and measured to realize Bell state measurements. The simplest linear optical Bell state measurement for photonic qubits succeeds probabilistically. When a successful optical Bell state measurement is performed on photons from two ions, it results in entanglement being heralded between the ions. The atomic states of the communication ions are then transferred or "swapped" to the memory ions by ion-ion gates based on Coulomb interactions such as the Molmer-Sorensen gate [37] to store entanglement over the long coherence times of the memory ions. The action of the swap gate $S_{c\to m}$ (where c and m labels denote the communication and memory ions, respectively) on a pair of entangled communication ions is given by

$$\begin{aligned} S_{c_1\to m_1}\otimes S_{c_2\to m_2}|\psi\rangle_{m_1}|\beta\rangle_{c_1c_2}|\psi\rangle_{m_2} \\ = |\psi\rangle_{c_1}|\beta\rangle_{m_1m_2}|\psi\rangle_{c_2}. \end{aligned} \tag{1}$$

Here, the various quantum states are : $|\beta\rangle_{c_1c_2}$ for the entangled communication ions, $|\psi\rangle_{m_i}$ for the memory ions before the linear optical entanglement swap, and $|\psi\rangle_{c_i}$ for the communication ions after the ion-ion swapping operation.

Finally, the entanglement swap operation between two entangled memory ion pairs $|\beta\rangle_{m_1m_2}$ and $|\beta\rangle_{m_3m_4}$, when ions m_2, m_3 are in the same DSTI module, is accomplished by a CNOT operation followed by X and Z basis measurements. This operation extends the range of entanglement by establishing entanglement between m_1 and m_4. It must be mentioned that the measurements considered here, are not ion-selective, but rather project all the ions present in the module. This forms an important consideration in designing repeater protocols with the DSTI modules.

Error model: The success probability of optically-mediated heralded entanglement generation between communication ions present at two adjacent repeater nodes is given by $p = \frac{1}{2}\eta_c^2\eta_d^2 e^{-\alpha L_0}$. Here, η_c is the collection and coupling efficiency for the optical elements, η_d is the efficiency of the detectors used in the Bell state measurement circuit, α is the fiber attenuation parameter, which is typically 0.2 dB/km at 1550 nm, and L_0 is the inter-repeater spacing (detector dark counts and frequency conversion inefficiencies are neglected in the present analysis, and will be considered in future works). When the communication ions are present at the same repeater node, but in different DSTI modules, the success probability is given by $p' = \frac{1}{2}\eta_c^2\eta_d^2$, where it is assumed that the losses in transmission are negligible. Moreover, the entangled state of the communication ions is generally modeled by a Werner state of fidelity parameter F_0, given by

$$\rho_{c_1,c_2} = F_0\Phi^+ + \frac{1-F_0}{3}\left(\Phi^- + \Psi^+ + \Psi^-\right), \tag{2}$$

where $\Phi^\pm = |\Phi^\pm\rangle\langle\Phi^\pm|$ and $\Psi^\pm = |\Psi^\pm\rangle\langle\Psi^\pm|$ are maximally entangled qubit Bell state density operators, with $|\Phi^\pm\rangle = (|0,1\rangle \pm |1,0\rangle)/2$ and $|\Psi^\pm\rangle = (|0,0\rangle \pm |1,1\rangle)/2$, and $\{|0\rangle, |1\rangle\}$ being the computational Z basis eigenstates of the qubits. The Werner state model accounts for errors in the communication ions that may be caused by the presence of dephasing noise in the photonic qubits that undergo optical Bell state measurement.

Errors in the swap gate are compactly modeled jointly for a pair of instances of swap gates acting on two entangled communication ions to store the entanglement in two memory ions. The model is a two-qubit Pauli channel acting on the initial entangled state of the two communication ions resulting in a noisy mapping onto two memory ions (see Santra et al. [29, Eq. 3] for details), and is described as

$$\rho_{m_1m_2} = (1-\epsilon_g)\rho_{c_1c_2} + \frac{\epsilon_g}{16}\sum_{k,k'=0}^{3}\sigma_{k'}\otimes\sigma_k\rho_{c_1c_2}\sigma_{k'}\otimes\sigma_k, \tag{3}$$

$$= F_i\Phi^+ + \frac{1-F_i}{3}\left(\Phi^- + \Psi^+ + \Psi^-\right), \tag{4}$$

$$F_i = (1-\epsilon_g)F_0 + \frac{\epsilon_g}{4}, \tag{5}$$

where $\{\sigma_k\}_{k=1,2,3}$ are the Pauli matrices X, Y and Z, the state $\rho_{c_1c_2}$ is the Werner state of (2) and ϵ_g is the error parameter associated with the swap gate.

Finally, imperfections in the entanglement swap operation are modeled in two parts, namely, errors associated with i) the CNOT gate, and ii) the X, Z measurement. i) The action of a noisy CNOT gate, also of error parameter ϵ_g, acting on two qubits m_2, m_3 initially in state $\rho_{m_2}\otimes\rho_{m_3}$, is modeled as

$$\begin{aligned} \rho'_{m_2m_3} = (1-\epsilon_g)\mathrm{CNOT}\left(\rho_{m_2}\otimes\rho_{m_3}\right)\mathrm{CNOT}^\dagger \\ + \epsilon_g\frac{I_{m_2m_3}}{4}, \end{aligned} \tag{6}$$

where m_2, m_3 are the control and the target qubits, respectively, for the CNOT operation and $I_{m_2m_3}$ is the two-qubit identity operator. Note that ϵ_g is an overestimate for the error in this gate, since it involves fewer Coulomb gates than the swap operation. ii) Errors associated with the X and Z measurements on the control and target qubits of the CNOT gate are functions of the gate error parameter ϵ_g and the initial fidelity of the entangled Werner state of two communication ions. When entanglement swaps are performed across a chain of n repeater nodes, the final noisy entangled state heralded between memory ions at the end nodes of the chain can be described also as a Werner state of the form in (2) with a fidelity parameter given by $F_f = 1 - \frac{3}{2}Q(n)$, where

$$Q(n) = \frac{1}{2}\left(1 - \left(1 - 2\epsilon_g - \frac{4}{3}(1-F_0)\right)^n\right). \tag{7}$$

Timing Parameters: The proposed repeater design has a few characteristic timing parameters that are summarized in Table I. Firstly, the clock cycle duration τ is the primary time unit, which denotes the rate at which the repeater nodes attempt ion-photon entanglement generation. Secondly, the gate and measurement times are assumed to be 100μs, at which speeds, e.g., high fidelity swap from ^{138}Ba$^+$ to ^{171}Yb$^+$ have been demonstrated [31, 32]. Thirdly, there are the lifetimes of the communication and memory ions. The former is taken to be 100μs (as has been reported for ^{138}Ba$^+$ ions), while the latter is assumed to be long; the lifetime of ^{171}Yb$^+$ transitions have been engineered to run in the order of minutes [38].

Timing Parameter	Associated Meaning
τ	Clock cycle duration
τ_g	Ion-ion gate and measurement times
τ_m	Memory ion lifetime
τ_o	Communication ion lifetime

Table I. Timing parameters associated with trapped ion repeaters.

III. REPEATER PROTOCOLS BASED ON SPATIAL AND TEMPORAL MULTIPLEXING

In this section, we provide a brief background on multiplexing-based repeater protocols. To begin with, due to the no-cloning theorem [39], unlike classical communication, the simple strategy of 'amplify and retransmit' is not physically viable for entanglement generation between two remote parties Alice and Bob. The rates for direct transmission of qubits over a M quantum channels with a source repetition rate of $1/\tau$ are limited by the repeaterless bound on the entanglement generation capacity, which for pure loss channels of transmissivity η, is given by [14]

$$C_{\text{direct}}(\eta, M, \tau) = -\frac{M}{\tau}\log_2(1-\eta) \text{ ebits/s}, \tag{8}$$

referred to as the PLOB bound hereinafter. The PLOB bound tends to be $\propto \eta$ for $\eta \ll 1$.

There are multiple paradigmatic approaches using quantum repeaters to beat this bound. A widely recognized classification of these approaches is in terms of the so-called *one-way* versus *two-way* repeaters. *One-way quantum repeaters* encode the transmitted qubits using error correcting codes and the task for quantum repeaters is to decode, correct for transmission errors, re-encode and transmit from pre-determined locations on the channel. Entanglement can be distributed using these repeaters by encoding and transmitting one share of a logically-encoded ebit through the repeater links. This is a similar strategy as repeaters for one way classical communication. *Two-way quantum repeaters*, on the other hand, rely on the generation of local entanglement on smaller segments of the network. These locally shared ebits are concatenated with the aid of entanglement swaps to eventually achieve shared entanglement between the end parties on the channel. Such protocols could potentially be interspersed with entanglement purification to improve the quality of the shared ebit that is ultimately generated.

In this work, we focus on two-way repeaters. Two-way repeaters are equipped with sources of photonic entangled pairs, quantum memory (QM) registers (trapped memory ions for our proposed designs in this work) and additional circuitry to perform quantum logic on the qubits stored in the QM register (including entanglement swaps on the memory ions). We begin with the assumption that the sources can produce perfect Bell pairs on demand every τ seconds. For simplicity, we initially assume arbitrarily large QM registers and infinitely long coherence times for the qubits stored in the QM. This is a necessary consideration for a constraint-free analysis of multiplexing.

For the simplest network design, namely a line network connecting two communicating parties, the total link distance L is divided into $n+1$ elementary links. The repeater stations occupy the nodes at either end of each elementary link in this segmented network. The core strategy of the protocol is to generate shared entanglement on the elementary links before attempting entanglement swaps (between QMs) internally in the repeater stations. This is achieved by performing a linear optical Bell state measurement (BSM) between the transmitted qubits from neighbouring repeater stations. The simplest linear optical BSM is a probabilistic operation, which has a probability $p \leq 1/2$ of succeeding. Note that p is dependent on the length of the elementary links, i.e. increasing the length of the elementary links deteriorates p. Since loss on fiber scales exponentially with distance, $p \propto \exp(-\alpha L/(n+1))$. Note that increasing n, i.e., reducing the elementary link length boosts p. However, this also means that a larger number of elementary links must simultaneously succeed, which shows a clear tradeoff. Futher we assume that the QM entanglement swap can succeed with a probability $q \leq 1$, where $q = 1$ is possible with high fidelity entanglement swapping gates for trapped ion qubits. The achievable rate is given by,

$$R_0(n) = \frac{p^{n+1} \times q^n}{\tau}. \tag{9}$$

Since $R_0(n) < e^{-\alpha L}/\tau$, we perform worse than with direct transmission.

However, with the aid of multiple parallel attempts, i.e., multiplexing, the entanglement generation rate can be engineered to surpass direct transmission. This is the natural strategy to consider when individual links can only be generated in a probabilistic manner; instead of independent single attempts succeeding simultaneously, we perform multiple parallel attempts for each elementary link and concatenate successful links. Spatial (or equivalently spectral) multiplexing is the easiest modification to this protocol which is based on this paradigm. Here, the design incorporates parallel channels spatially, i.e., with separate optical fibers. With this modification, instead of a single BSM attempt every time slot, we can perform M attempts and look for one success. With a spatial multiplexing size of M, the entanglement generation rate is now given by,

$$R_1(n) = \frac{(1-(1-p)^M)^{n+1} \times q^n}{\tau}. \tag{10}$$

It has been shown that with optimal choice of n and suitable M, the rate equation in Eqn. (10) can surpass the direct transmission PLOB bound at a given link length. In fact, the rate envelope for Eqn. (10) has been derived in [40], and has been shown to scale as $R_1 \propto e^{-s\alpha L}$ with $s < 1$, which allows the protocol to surpass rates possible with direct transmission.

Another strategy for multiplexing is to accumulate successes from m attempts over blocks of the fundamental time slot of τ seconds. This is called time multiplexing and mimics the effect of using multiple channels without the necessity for additional physical channels. Hence, we can perform the entanglement swap between different QMs at a repeater node only after every m time slots. The entanglement generation rate for the time multiplexed protocol is given by

$$R_2(n,m) = \frac{(1-(1-p)^m)^{n+1} \times q^n}{m\tau}. \tag{11}$$

It has been shown in [25, 41] that a time-multiplexed protocol can achieve a sub-exponential rate-vs.-distance scaling i.e. $R_2 \propto e^{-t\sqrt{\alpha L}}$ with $t < 1$. This is an improved performance over spatial multiplexing, and it has been shown that a protocol may surpass the PLOB bound with just time multiplexing. However, in a practical implementation, time multiplexing requires highly reliable QMs and large switching trees that scale as $\log_2(m)$. Imperfections in these components can lead to the loss of the sub-exponential advantage [25]. In general, with the incorporation of both spatial and temporal multiplexing, a two-way repeater protocol can achieve the rate $R(L,n,m)$ given as

$$R(L,n,m) = \frac{(1-(1-p)^{mM})^{n+1} \times q^n}{m\tau}. \tag{12}$$

It is important to note that there is a key difference between the multiplexing degrees in the spatial (M) and time (m) strategies. Increasing M in a spatially multiplexed protocol requires the use of additional channels, which may be highly constrained (i.e. we may be limited by the number of physical optical fibers). In fact it is generally something that the network architect cannot modify, and hence it is not practical to optimize the rate with respect to M. Rather, given a certain maximum value of M, the rate envelope, as derived in Ref. [40], gives us an idea about the viability of the protocol to surpass the PLOB bound. Increasing the time multiplexing degree m is only governed by the lifetime of the QM. As long as the lifetime surpasses a certain threshold governed by the protocol design, we can modify m without the need for additional resources. Unlike spatial multiplexing, time multiplexing can boost the probability of link creation on the elementary link seemingly arbitrarily, by increasing m. However, by increasing m, the effective time step increases from τ to $m\tau$ which degrades the rate (see (11)). The boost in the success probability of the link, along with the optimization of the number of QR nodes n, overcompensates degradation, and an optimal value of m for a given L achieves the sub-exponential scaling.

Note that the protocols we consider in this work fall in the class of so-called second generation repeaters in the classification of successive generations of repeaters, since they do not include intermediate, iterative entanglement distillation steps.

IV. MULTIPLEXING-BASED PROTOCOLS FOR TRAPPED-ION REPEATERS: PROPOSED DESIGNS AND EVALUATION

In this section, we present the proposed protocols based on spatial and time multiplexing for entanglement distribution across a line network of trapped-ion repeaters, where the repeater nodes are as described in Sec. II. The protocols leverage the multiple communication ions present within each DSTI module at each repeater node for multiplexed entanglement generation attempts across elementary links in the network. The fundamental time step τ, or in other words, the clock cycle duration, multiples of which are used as time multiplexing blocks, is chosen as a free parameter, and not tied to the physical distance between the repeaters. This makes our protocols more general than the ones presented in Ref. [29].

The network layer parameters used in defining our protocols and the resource parameters to support the network protocols, are listed in Tables II and III, respectively.

Parameter	Associated Meaning
L_0	Inter-repeater spacing
M	Degree of spatial multiplexing
m	Degree of time multiplexing

Table II. Network-layer protocol parameters.

Parameter	Associated Meaning
s	DSTI modules per repeater
N_o	$^{138}Ba^+$ ions per DSTI module
N_m	$^{171}Yb^+$ ions per DSTI module

Table III. Resource parameters.

Let us consider the simplest case, where there is a single DSTI module at each repeater, i.e., $s = 1$. Consider a (m, M) repeater protocol with spatial multiplexing $M \geq 1$ and time multiplexing $m \geq 1$ implemented over n equally spaced repeaters and a total distance L (between two communicating parties). The inter-repeater spacing is given by $L_0 = L/(n+1)$. For a given L_0, the time it takes for the heralding information of success or failure of optically-mediated entanglement generation across adjacent repeater nodes to arrive at the nodes is $T = L_0/c$, where c is the speed of light in the optical fiber used for inter-repeater node transmissions (henceforth referred to as the heralding time). The protocol aims to successfully herald at least one elementary link entanglement in each elementary link from $m \times M$ total attempts spread over $m\tau$ seconds. The heralding time and the gates and measurement time together add up to dictate the rate of generating the elementary link entanglements. Since all the memory ions are in one DSTI module, entanglement swapping across these elementary link entangled memory ions can subsequently be performed deterministically using CNOT gate followed by X and Z measurement to distribute entanglement between the end nodes.

Rate Formulas under ideal repeater operations. Assuming gate operations at the repeaters to be ideal and the optical fibers to be pure loss channels (no dephasinng errors) for the moment, the rate in ebits per second attained by the protocol is given by the general formula

$$R = \frac{\left(1 - (1-p)^{Mm}\right)^{n+1}}{\mathbf{T}}, \tag{13}$$

where the numerator denotes the probability of successfully heralding at least one entangled ion-ion pair across each of the $n+1$ elementary links (p being the success probability of optical Bell swap discussed in Sec. II), and the $\mathbf{T}$ in the denominator is the time it takes to complete m time steps of entanglement generation attempts across the elementary links. In order to attain optimal rates at any distance L, an optimal number of repeaters n_{opt} would be required to be placed along the distance. Too few repeaters would result in excessive errors due to photon loss, whereas too many repeaters would result in excessive operational errors at the repeater nodes.

Notice that the rate in Eqn. (13) is a function of the parameters m, M, and n along with physical system parameters such as collection and detection efficiencies η_c, η_d and the total distance L that enter the formula through $p = \frac{1}{2}\eta_c^2\eta_d^2 e^{-\alpha L_0}$, where $L_0 = L/n$. The denominator $\mathbf{T}$ is a function of the time multiplexing block length m and the clock cycle duration τ, but also depends on the ion-ion gate and measurement times τ_g and the heralding time T, which is in turn a function of L_0. The dependence on τ_g is due to the fact that it takes a non-zero amount of time to perform the essential entanglement swap operations at the repeater nodes, which is $2\tau_g$ seconds (τ_g for the CNOT gate and τ_g for the X, Z measurements).

The precise formula for the rate attainable with an (m, M) repeater protocol over n repeaters placed along a total distance L, along with the ion requirements to support the protocol are tabulated in Table IV. They depend on the relative values of the heralding time T, ion-ion gate times τ_g and the communication ion lifetime τ_o. For simplicity of analysis, let us consider T to be $T = k\tau$ and the $\tau_g = j\tau$, where τ is the clock cycle duration for ion-photon entanglement generation attempts at the nodes and $j, k \in \mathbb{Z}^+$. The parameter τ is a free parameter that can be chosen to be smaller than the ion-ion gate times, i.e., the time it takes to free up a communication ion for reuse after swapping its atomic state in to a memory ion. We assume that batches of communication ions placed in distinct sectors of the trap can be globally excited at each time step, and that there are as many sectors as the ratio $j = \tau_g/\tau$, so that they can be excited in a cyclic fashion to support the clock rate $1/\tau$. Most importantly, τ can be chosen independently of the heralding time, which distinguishes our protocol from the one presented in Ref. [29]. It is also implicitly and reasonably assumed that i) $\tau_o > \tau_g$ so that a communication ion's quantum state can be faithfully transferred to a memory ion with ion-ion gates before it irrecoverably decoheres, and ii) $\tau_m \gg m\tau$ for a larger range of values m, so that the memory ions can be considered to be noise free. Among the $6 = \binom{3}{2}$ orderings of the relative values of T, τ_g and τ_o, due to the reasonable assumption $\tau_o > \tau_g$, we are left with 3 possible orderings, namely: $T \geq \tau_o > \tau_g$, $\tau_o > T \geq \tau_g$ and $\tau_o > \tau_g > T$. Table IV discusses the rates and the ion requirements for each of these cases. Timing charts and timing diagrams that describe the operations at the repeater nodes from time-step to time-step under these different conditions are elucidated in Appendix A.

Table V in the Appendix describes the case $T \geq \tau_0 > \tau_g$. In this scenario, at every time step, $2M$ communication ions generate ion-photon entanglement, with M of the photons being directed towards the left of the node and the other M towards the right of the node. The moment these photons are generated, an ion-ion gate is initiated on each of the communication ions, to swap their atomic state into memory ions. The gate time is taken to be $j\tau, j \in \mathbb{Z}^+$ for simplicity. At time $t = j\tau$, the communication ions that were used to generate ion-photon entanglement at time step $t = 0$ are freed up due to the completion of the ion-ion gate, and hence are ready to be reused. At this point, the first $2M$ atomic states have been loaded into memory ions. At time step $t = k\tau$, the information about which two (one to the left of the node and one to the right), if any, of the $2M$ entanglement generation attempts at time $t = 0$ actually heralded an elementary link entanglement, is received, at which point, the other $2(M-1)$ memory ions are freed up and ready for reuse. At time $t = (k+m-1)\tau$, similarly, all potentially successfully heralded elementary link entanglements across the time multiplexing block length of m are stored in the memory ions. At this point, the

Table A	Criterion: $T \geq \tau_o > \tau_g$	Required N_o	Required N_m	Rate
		$2Mj$	$\leq 2Mm$	$\frac{\left(1-(1-p)^{Mm}\right)^{n+1}}{(k+m+2j-1)\tau}$
Table B	Criterion: $\tau_o > T > \tau_g$	Required N_o	Required N_m	Rate
	Case 1 $(k+j)\tau > \tau_o > k\tau$	Same as Table A		
	Case 2 $\tau_o > (k+j)\tau > k\tau$	$2(Mk+j)$	$2m$	$\frac{\left(1-(1-p)^{Mm}\right)^{n+1}}{(k+m+3j-1)\tau}$
Table C	Criterion: $\tau_o > \tau_g > T$	Required N_o	Required N_m	Rate
	Case 1 $(k+j)\tau > \tau_o > j\tau$	$2Mj$	$\leq 2Mm$	$\frac{\left(1-(1-p)^{Mm}\right)^{n+1}}{(m+3j-1)\tau}$
	Case 2 $\tau_o > (k+j)\tau > j\tau$	Same as Table B, Case 2		

Table IV. Rates and ion requirements for $s = 1$ operation of the (m, M) multiplexed repeater protocol. The rate expressions correspond to ideal gate operations, and the optical fibers are assumed to be a pure loss channel. See Appendix A for detailed timing charts and corresponding timing diagrams.

repeater nodes choose the latest successful heralded link to the left and to the right and perform entanglement swap on those corresponding memory ions. Performing the entanglement swap involves measuring these memory ions and takes $2\tau_g = 2j\tau$. Thus, the rate of distributing 1 ebit across the end nodes of the trapped-ion repeater chain is $\propto 1/(k+m-1+2j)\tau$. Since we consider global measurements that measure all ions in the DSTI, all the other accumulated entanglement resources at the nodes are also cleared in the process. The protocol then starts once again from time step $t = 0$.

Note that typically with time-multiplexed repeaters the heralding time only causes latency in the protocol without affecting the rates [25]. However, in the present scheme of trapped-ion repeaters, as mentioned above, ion measurements are considered to be global, full-trap measurements that measure all ions present in a DSTI, as opposed to measurement of individual ions in a trap. As a result, all the other accumulated entangled resources at the nodes are also cleared in the process, which impacts the entanglement distribution rates.

Rate Formulas under realistic (noisy) gate operations. When realistic noisy operations are considered at the repeater nodes, the rate formulas in Table IV get scaled by the distillable entanglement generation of the noisy end-to-end entangled state ρ_{AB} across the line repeater network. The noisy entangled state is given by a Werner state of fidelity parameter $F = 1 - \frac{3}{2}Q(n)$, where $Q(n)$ is as given in Eqn. 7. A lower bound on the distillable entanglement is given by the reverse coherent information of the state ρ_{AB}, defined as $I_R(\rho_{AB}) := H(B)_\rho - H(AB)_\rho$, where $H(B)_\rho = -\mathrm{Tr}(\rho_B \log_2 \rho_B)$ is the von Neumann entropy of ρ_B. For Bell diagonal states, and hence for Werner states, I_R can be easily computed, since ρ_B is the maximally mixed state of entropy $H(B)_\rho = 1$ and the entropy $H(AB)_\rho = -F \log_2 F - (1-F) \log_2 \frac{1-F}{3}$.

Ion Requirements: Once again, for the case $T \geq \tau_0 \geq \tau_g$, the ion requirements can be identified from the timing chart in Table V. The requirement on the number of communication ions is $2jM$, which is the value at which freed ions begin getting reused and the number of loaded Ba^+ ions saturates. In other words, $2jM$ Ba^+ ions are sufficient to support the optimal (m, M) repeater protocol. The maximum number of memory ions required in this case is given by $2mM$. The actual number could be smaller, depending on the value of m and its relation to j, k, which might allow for some freed memory ions to be reused. On the other hand, for the cases where $\tau_o > (k+j)\tau$, the optical ion requirement is $2(Mk+j)$, whereas the memory ion requirement is independent of M, and given by $2m$. This is because the large τ_o allows one to wait for the heralding information and subsequently apply the swap gate only between the successfully heralded communication ion and the corresponding memory ions.

Numerical Results: Firstly, we analyze the rate-vs.-distance trade-off. The operating parameters of the repeater are considered to be $\tau = 1\mu$s, $\tau_g = 1\mu$s (i.e., j=1), $\tau_o = 100\mu$s, $\eta_c = 0.3, \eta_d = 0.8$, and the inter-repeater transmissions are assumed to be over optical fiber of attenuation $\alpha = 0.2$ dB/km. The operational errors in gates and measurements are varied from 0 (for ideal repeaters) to $10^{-4}, 10^{-3}$ (with noisy operations). Different values of spatial multiplexing $M = 1, 5, 10$ are considered. The rates are numerically optimized over the time multiplexing block length m and the number of repeaters, where it is assumed that $\tau_o \gg m\tau$. The optimal rates were determined as the maximum of the optimal values of the different rate expressions in Table IV and are plotted in Fig. 2. The rates are found to show sub-exponential decay with respect to distance, primarily owing to deterministic entanglement swapping and additionally due to

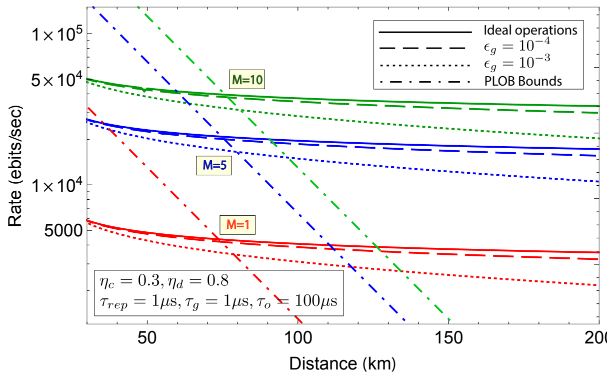

Figure 2. Entanglement distribution rate as a function of total distance optimized over the number of repeater nodes and the degree of time multiplexing, for different values of spatial multiplexing M, noise parameter ϵ_g, and $\tau_g = \tau = 1\mu s$. These rates are compared against the direct transmission benchmark, namely the corresponding PLOB bounds (dotdashed lines) given by $-\frac{M}{\tau}\log_2(1-\eta)$.

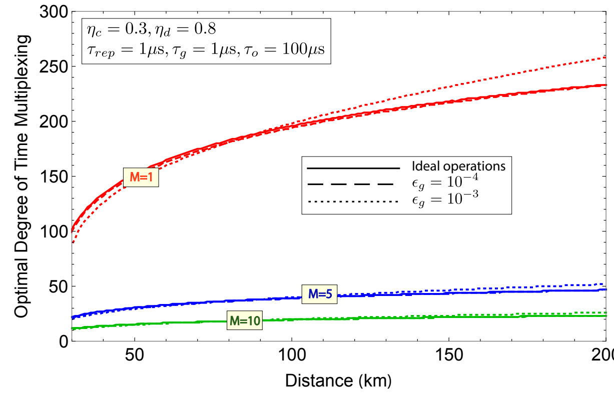

Figure 3. Optimal degree of time multiplexing as a function of total distance for different values of spatial multiplexing M, noise parameter ϵ_g, $\tau_g = \tau = 1\mu s$, and optimal number of repeaters.

time multiplexing. The rates are higher for higher M, but the advantage over the corresponding PLOB bounds calculated as per Eqn. 8 also occurs at commensurately longer distances. In the presence of operational errors in the repeaters, the degradation of the rates with distance rises with increasing values of the noise parameter, but the rates are independent of spatial multiplexing. Nevertheless, the rate-distance trade-off still beats the PLOB bound.

The optimal time multiplexing block-length and the optimal number of repeaters for different degrees of spatial multiplexing are plotted as functions of the total distance in Figs. 3 and 4, respectively. Notice that the optimal value of m increases with distance, and more so with increasing noise in the gates and measurements. Most importantly, the values of m are higher for the lower value of M. In fact, at any given distance L, when M is varied, the optimal m (m_{opt}) satisfies the same mode multiplexing product $\mathbf{m} = m \times M$. For a total distance of 150 km and noise parameter $\epsilon_g < 10^{-4}$, the optimal product is found to be $\mathbf{m}_{\text{opt}} \approx 220$. Hence, for $M = 1, 5, 10$, we have $m_{\text{opt}} = 220, 44, 22$, respectively. The optimal number of repeaters is seen to grow with the total distance. It is found to be nearly independent of M, but naturally slows down with increasing gate and measurement noise, as more QR nodes would add more noise to the shared ebits. For a total distance of $L = 150$ km, and at an optimistic value of the noise parameter $\epsilon_g = 10^{-4}$, the optimal number of repeaters is found to be 25, which amounts to an inter-repeater spacing $L_0 \approx 6$ km. This is similar to the optimal spacing identified in [29].

The number of communication and memory ions per repeater node (N_o, N_m) required to support the optimal rates under the proposed mode-multiplexing protocols are shown in Figs. 5 and 6, respectively. The value of N_o decreases sub-exponentially with distance so long as

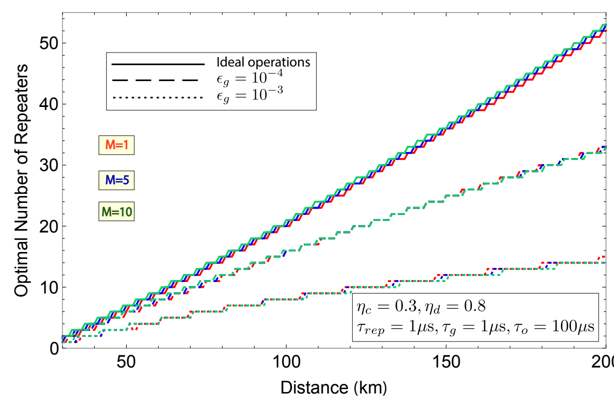

Figure 4. Optimal number of repeater nodes as a function of total distance for different values of spatial multiplexing M, noise parameter ϵ_g, $\tau_g = \tau = 1\mu s$ and optimal time multiplexing.

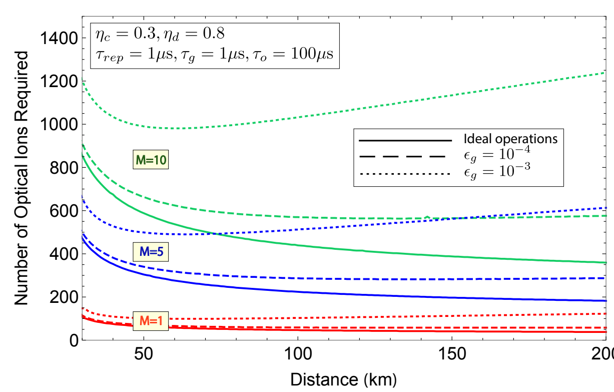

Figure 5. Required number of optical ions as a function of total distance for different values of spatial multiplexing M, noise parameter ϵ_g, $\tau_g = \tau = 1\mu s$ and optimal number of repeaters and time multiplexing.

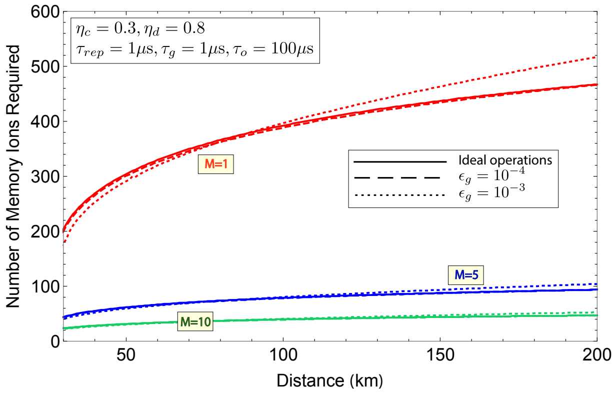

Figure 6. Required number of memory ions as a function of total distance for different values of spatial multiplexing M, noise parameter ϵ_g, $\tau_g = \tau = 1\mu$s and optimal number of repeaters and time multiplexing.

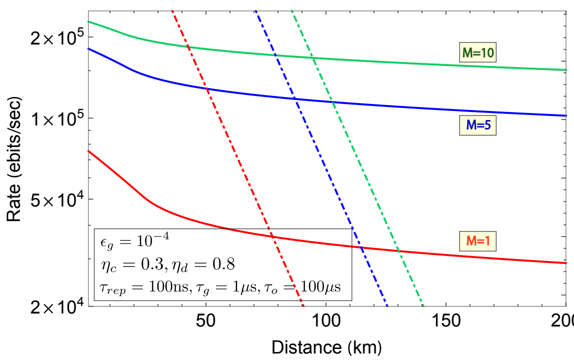

Figure 7. Entanglement distribution rate as a function of total distance optimized over the number of repeater nodes and the degree of time multiplexing, for different values of spatial multiplexing M, with realistic noisy gate operations of infidelity $\epsilon_g = 10^{-4}$ and $\tau_g = 10\tau = 1\mu$s. These rates are compared against the direct transmission benchmark, namely the corresponding PLOB bounds (dot dashed lines) given by $-\frac{M}{\tau}\log_2(1-\eta)$.

the gate and measurement noise ϵ_g is small. In such a scenario, the required numbers are smallest for protocols with smaller M and increases with M. The value of N_o tends to non-monotonically increase with distance for ϵ_g above a threshold. This is because large ϵ_g drives down the optimal number of repeaters and consequently drives up the inter-repeater spacing. With increasing inter-repeater spacing, the proposed protocol chooses to operate under Table IV B and C, Case 2, where the nodes try to save on the required number of memory ions, at the expense of more optical ions. On the other hand, the required number memory ions always increases with distance, since the optimal time multiplexing blocklength m increases, too, and the required number of memory ions is proportional to m. It is higher for lower values of M (or in other words for higher values of m).

Fig. 7 plots the entanglement distribution rates when $\tau = 100$ns, while $\tau_g = 1\mu$s, i.e., for $j = 10$. With the order of magnitude faster ion-photon entanglement generation attempts, the rates are seen to increase commensurately by an order of magnitude. The rate increase, as expected, comes at the cost of commensurately increased number of ions in the DSTI modules that are required. Also, it necessitates engineering traps with distinct sectors of ions that can be cyclically excited to support ion-photon entanglement generation attempts at the higher clock rate.

V. DISCUSSION AND CONCLUSION

We note that the rates in Fig. 2 based on the protocols in Sec. IV are higher than those reported in ref. [29, Fig. 7(b)]. For instance, at a total distance of 150 km, noise parameter $\epsilon_g = 10^{-4}$ and all other parameters being identical, our protocol with $M = 10$ spatial multiplexing attains 40000 ebits/sec, whereas the protocol in ref. [29] achieves 800 ebits/s. However, the rate enhancement comes at the cost of higher ion number requirements. At a total distance of 150 km and with $\epsilon_g = 10^{-4}$, the required number of optical ions and memory ions are $N_o = 600, 300, 50$, and $N_m = 40, 80, 420$, for $M = 10, 5, 1$, respectively, whereas the protocol in ref. [29], only required $N_o = 1, N_m = 2$ for $M = 1$ and $N_o = 10, N_m = 2$ for $M = 10$. It should be interesting to analyze the optimal rate-vs-distance performance of the proposed protocols while considering ion costs, similar to the Rate/ion analysis performed in Ref. [29]. Similarly, it will be interesting to consider constrained optimization problems for the rates under the proposed protocols, where i) the number of communication and memory ions at each repeater node is constrained, and ii) where the total number of communication and memory ions across all the repeater nodes is constrained.

The relatively large number requirements can be attained by bootstrapping multiple DSTI modules. However, that would require optically-mediated entanglement swapping operations, which will no longer be deterministic and in turn cause a degradation of entanglement distribution rates. More general protocols can be designed that optimally leverage multiple DSTI modules at repeater nodes, and are a work in progress.

In conclusion, we presented a general architecture for a repeater node based on DSTI modules, and discussed repeater protocols based on spatial and time multiplexing. For DSTI modules with $^{138}Ba^+$ as communication ions and $^{171}Yb^+$ as memory ions, assuming operation errors under $\epsilon_g < 10^{-4}$, the proposed repeater protocols based on spatial and time multiplexing can attain entanglement distribution rates ~ 40000 ebits/s at a distance of 150 km, with repeaters placed at ≈ 6 km spacing and each containing about 600 and 40 $^{138}Ba^+$ and $^{171}Yb^+$ ions, respectively. These rates are higher than the ones reported in earlier works, but require larger number of ions at the repeater nodes. Nevertheless, the required number of ions will soon be within reach of trapped-ion technologies.

ACKNOWLEDGMENTS

This work was supported by the National Science Foundation (NSF) Convergence Accelerator Program, award number 2040695. KPS thanks Liang Jiang for helpful discussions.

[1] Ivan H Deutsch. Harnessing the power of the second quantum revolution. PRX Quantum, 1(2):020101, November 2020.

[2] Jonathan P Dowling and Gerard J Milburn. Quantum technology: the second quantum revolution. Philos. Trans. A Math. Phys. Eng. Sci., 361(1809):1655–1674, August 2003.

[3] Kishor Bharti, Alba Cervera-Lierta, Thi Ha Kyaw, Tobias Haug, Sumner Alperin-Lea, Abhinav Anand, Matthias Degroote, Hermanni Heimonen, Jakob S Kottmann, Tim Menke, Wai-Keong Mok, Sukin Sim, Leong-Chuan Kwek, and Alán Aspuru-Guzik. Noisy intermediate-scale quantum (NISQ) algorithms. January 2021.

[4] F Xu, X Ma, Q Zhang, H K Lo, and J W Pan. Secure quantum key distribution with realistic devices. Rev. Mod. Phys., 2020.

[5] Zheshen Zhang and Quntao Zhuang. Distributed quantum sensing. Quantum Sci. Technol., December 2020.

[6] Morten Kjaergaard, Mollie E Schwartz, Jochen Braumüller, Philip Krantz, Joel I-J Wang, Simon Gustavsson, and William D Oliver. Superconducting qubits: Current state of play. Annu. Rev. Condens. Matter Phys., 11(1):369–395, March 2020.

[7] Sébastien Pezzagna and Jan Meijer. Quantum computer based on color centers in diamond. Applied Physics Reviews, 8(1):011308, March 2021.

[8] Colin D Bruzewicz, John Chiaverini, Robert McConnell, and Jeremy M Sage. Trapped-ion quantum computing: Progress and challenges. Applied Physics Reviews, 6(2):021314, June 2019.

[9] Fulvio Flamini, Nicolò Spagnolo, and Fabio Sciarrino. Photonic quantum information processing: a review. Rep. Prog. Phys., 82(1):016001, January 2019.

[10] Ryszard Horodecki, Paweł Horodecki, Michał Horodecki, and Karol Horodecki. Quantum entanglement. Rev. Mod. Phys., 81(2):865–942, June 2009.

[11] Stephanie Wehner, David Elkouss, and Ronald Hanson. Quantum internet: A vision for the road ahead. Science, 362(6412), October 2018.

[12] Stefano Pirandola and Samuel L Braunstein. Physics: Unite to build a quantum internet. Nature, 532(7598):169–171, April 2016.

[13] H J Kimble. The quantum internet. Nature, 453(7198):1023–1030, June 2008.

[14] Stefano Pirandola, Riccardo Laurenza, Carlo Ottaviani, and Leonardo Banchi. Fundamental limits of repeaterless quantum communications. Nat. Commun., 8:15043, April 2017.

[15] Masahiro Takeoka, Saikat Guha, and Mark M Wilde. Fundamental rate-loss tradeoff for optical quantum key distribution. Nat. Commun., 5:5235, October 2014.

[16] H-J Briegel, W Dür, J I Cirac, and P Zoller. Quantum repeaters: The role of imperfect local operations in quantum communication. Phys. Rev. Lett., 81(26):5932–5935, December 1998.

[17] William J Munro, Koji Azuma, Kiyoshi Tamaki, and Kae Nemoto. Inside quantum repeaters. IEEE J. Sel. Top. Quantum Electron., 21(3):78–90, May 2015.

[18] Masoud Ghalaii and Stefano Pirandola. Capacity-approaching quantum repeaters for quantum communications. Phys. Rev. A, 102(6):062412, December 2020.

[19] Josephine Dias, Matthew S Winnel, Nedasadat Hosseinidehaj, and Timothy C Ralph. Quantum repeater for continuous-variable entanglement distribution. Phys. Rev. A, 102(5):052425, November 2020.

[20] Kaushik P Seshadreesan, Hari Krovi, and Saikat Guha. Continuous-variable quantum repeater based on quantum scissors and mode multiplexing, 2020.

[21] Peter Loock, Wolfgang Alt, Christoph Becher, Oliver Benson, Holger Boche, Christian Deppe, Jürgen Eschner, Sven Höfling, Dieter Meschede, Peter Michler, Frank Schmidt, and Harald Weinfurter. Extending quantum links: Modules for fiber and memory based quantum repeaters. Adv. Quantum Technol., 3(11):1900141, November 2020.

[22] Nicolas Sangouard, Christoph Simon, Hugues de Riedmatten, and Nicolas Gisin. Quantum repeaters based on atomic ensembles and linear optics. Rev. Mod. Phys., 83(1):33–80, March 2011.

[23] L Childress, J M Taylor, A S Sørensen, and M D Lukin. Fault-tolerant quantum repeaters with minimal physical resources and implementations based on single-photon emitters. Phys. Rev. A, 72(5):052330, November 2005.

[24] Sreraman Muralidharan, Linshu Li, Jungsang Kim, Norbert Lütkenhaus, Mikhail D Lukin, and Liang Jiang. Optimal architectures for long distance quantum communication. Sci. Rep., 6:20463, February 2016.

[25] P. Dhara, A. Patil, H. Krovi, and S. Guha. Subexponential rate versus distance with time multiplexed quantum repeaters. arXiv:2105.01002, 2021.

[26] Christopher Monroe. Quantum networks with trapped ions, 2007.

[27] C Monroe and J Kim. Scaling the ion trap quantum processor. Science, 339(6124):1164–1169, March 2013.

[28] Nicolas Sangouard, Romain Dubessy, and Christoph Simon. Quantum repeaters based on single trapped ions. Phys. Rev. A, 79(4):042340, April 2009.

[29] Siddhartha Santra, Sreraman Muralidharan, Martin Lichtman, Liang Jiang, Christopher Monroe, and Vladimir S Malinovsky. Quantum repeaters based on two species trapped ions. New J. Phys., 21(7):073002, July 2019.

[30] W P Grice. Arbitrarily complete bell-state measurement using only linear optical elements. Phys. Rev. A, 84(4):042331, October 2011.

[31] I V Inlek, C Crocker, M Lichtman, K Sosnova, and C Monroe. Multispecies Trapped-Ion node for quantum networking. Phys. Rev. Lett., 118(25):250502, June 2017.
[32] T R Tan, J P Gaebler, Y Lin, Y Wan, R Bowler, D Leibfried, and D J Wineland. Multi-element logic gates for trapped-ion qubits. Nature, 528(7582):380–383, December 2015.
[33] Yuan Lee, Eric Bersin, Axel Dahlberg, Stephanie Wehner, and Dirk Englund. A quantum router architecture for high-fidelity entanglement flows in multi-user quantum networks. arXiv preprint arXiv:2005. 01852, 3, 2020.
[34] Stefan Krastanov, Hamza Raniwala, Jeffrey Holzgrafe, Kurt Jacobs, Marko Lončar, Matthew J Reagor, and Dirk R Englund. Optically-Heralded entanglement of superconducting systems in quantum networks. December 2020.
[35] John Hannegan, Uday Saha, James D Siverns, Jake Cassell, Edo Waks, and Qudsia Quraishi. C-band single photons from a trapped ion via two-stage frequency conversion. March 2021.
[36] James D Siverns, John Hannegan, and Qudsia Quraishi. Neutral-Atom Wavelength-Compatible 780 nm single photons from a trapped ion via quantum frequency conversion, 2019.
[37] Klaus Molmer and Anders Sorensen. Multiparticle Entanglement of Hot Trapped Ions. Physical Review Letters, 82(9):1835–1838, March 1999.
[38] Ye Wang, Mark Um, Junhua Zhang, Shuoming An, Ming Lyu, Jing-Ning Zhang, L.-M. Duan, Dahyun Yum, and Kihwan Kim. Single-qubit quantum memory exceeding ten-minute coherence time. Nature Photonics, 11(10):646–650, October 2017.
[39] W K Wootters and W H Zurek. A single quantum cannot be cloned. Nature, 299(5886):802–803, October 1982.
[40] S. Guha, H. Krovi, C. A. Fuchs, Z. Dutton, J. A. Slater, C. Simon, and W. Tittel. Rate-loss analysis of an efficient quantum repeater architecture. Phys. Rev. A, 92(2):022357, August 2015.
[41] M. Razavi, M. Piani, and N. Lutkenhaus. Quantum repeaters with imperfect memories: Cost and scalability. Phys. Rev. A, 80(3):032301, September 2009.

Appendix A: Timing Analysis for Resource Count Calculation

There are multiple operating regimes for realistic operations with noisy and non-instantaneous quantum gates. The reader may refer to Table IV for a summary of the various protocol types. We have examined the timing analysis of each protocol type in depth in Tables V-VII. The corresponding timing diagrams are shown in Figs. 8-11

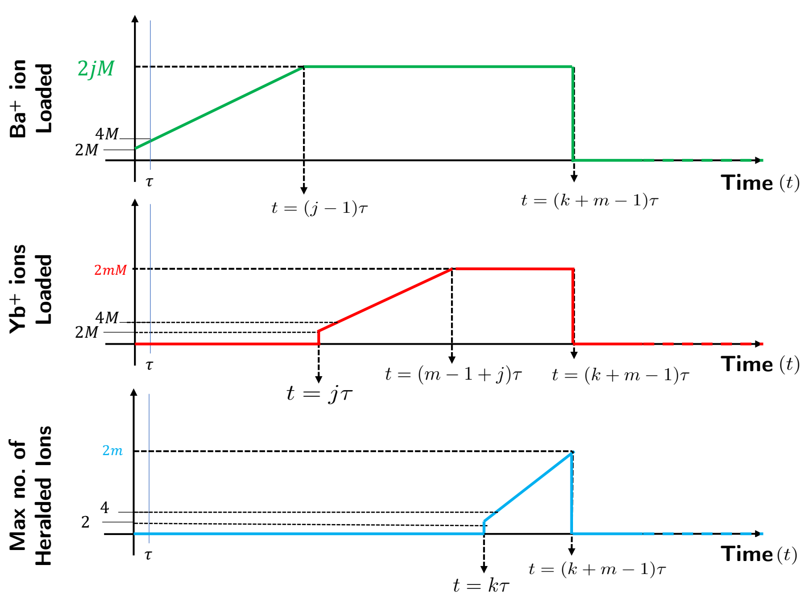

Figure 8. Timing diagram for Table I Type A Case 1

Appendix B: Optimization Process

Since the protocols listed in Section IV are determined by relation between the timing parameters, it is not directly apparent, which rate equation holds true for a given set of network-layer protocol parameters (refer Table II). The number of repeaters plays a primarily role in determining the herlding time T. For the present numerical analysis, we find the optimal parameter values for a given set of conditions using standard optimization techniques. Depending on

Case 1	Ba^+ Occupancy			Yb^+ Occupancy		Max. number of heralded ions
Time	Initialized	Freed	Loaded	Loaded	Freed	
0	$2M$	-	$2M$	-	-	-
τ	$4M$	-	$4M$	-	-	-
$\vdots$	$\vdots$	$\vdots$	$\vdots$	$\vdots$	$\vdots$	$\vdots$
$(j-1)\tau$	$2jM$	-	**2jM**	-	-	-
$j\tau$	$2(j+1)M$	$2M$	$2jM$	$2M$	-	-
$\vdots$	$\vdots$	$\vdots$	$\vdots$	$\vdots$	$\vdots$	$\vdots$
$(m-1+j)\tau$	$2(m+j)M$	$2mM$	$2jM$	**2mM**	-	-
$\vdots$	$\vdots$	$\vdots$	$\vdots$	$\vdots$	$\vdots$	$\vdots$
$k\tau$	$2(k+1)M$	$2(k-j+1)M$	$2jM$	$2(k-j+1)M$	$2(M-1)$	2
$\vdots$	$\vdots$	$\vdots$	$\vdots$	$\vdots$	$\vdots$	$\vdots$
$(\mathbf{k}+\mathbf{m}-\mathbf{1})\tau$	$2(k+m)M$	$2(k+m-j)M$	$2jM$	$2(k+m-j)M$	$2m(M-1)$	**2m**

Case 2	Ba^+ Occupancy			Yb^+ Occupancy		Max. number of heralded ions
Time	Initialized	Freed	Loaded	Loaded	Freed	
0	$2M$	-	$2M$	-	-	-
τ	$4M$	-	$4M$	-	-	-
$\vdots$	$\vdots$	$\vdots$	$\vdots$	$\vdots$	$\vdots$	$\vdots$
$(j-1)\tau$	$2jM$	-	**2jM**	-	-	-
$j\tau$	$2(j+1)M$	$2M$	$2jM$	$2M$	-	-
$\vdots$	$\vdots$	$\vdots$	$\vdots$	$\vdots$	$\vdots$	$\vdots$
$k\tau$	$2(k+1)M$	$2(k-j+1)M$	$2jM$	$2(k-j+1)M$	$2(M-1)$	2
$\vdots$	$\vdots$	$\vdots$	$\vdots$	$\vdots$	$\vdots$	$\vdots$
$(m-1+j)\tau$	$2(m+j)M$	$2mM$	$2jM$	**2mM**	$2(m+j-k)(M-1)$	$2(m+j-k)$
$\vdots$	$\vdots$	$\vdots$	$\vdots$	$\vdots$	$\vdots$	$\vdots$
$(\mathbf{k}+\mathbf{m}-\mathbf{1})\tau$	$2(k+m)M$	$2(k+m-j)M$	$2jM$	$2(k+m-j)M$	$2m(M-1)$	**2m**

Table V. Timing chart for Table IV Type A, i.e., when $k\tau \geq \tau_o > j\tau$, and Table IV B Case 1, i.e., $(\tau_o > k\tau > j\tau) \wedge ((k+j)\tau > \tau_0 > k\tau)$. Both of these involve sub-cases 1 and 2 corresponding to $k-j+1 > m$ and $k-j+1 < m$, respectively. The timing diagrams for the different cases of this protocol type are shown in Figs. 8 and 9

the optimal values calculated, we now have to make a decision about which type of the rate equation from Table IV is actually applicable. This is done by traversing the decision tree for the optimal parameter values shown in Fig. 12. One can note that based on the conditions (red diamonds) that are satisfied, the end leaves of the decision tree indicate which rate equation holds true (blue boxes).

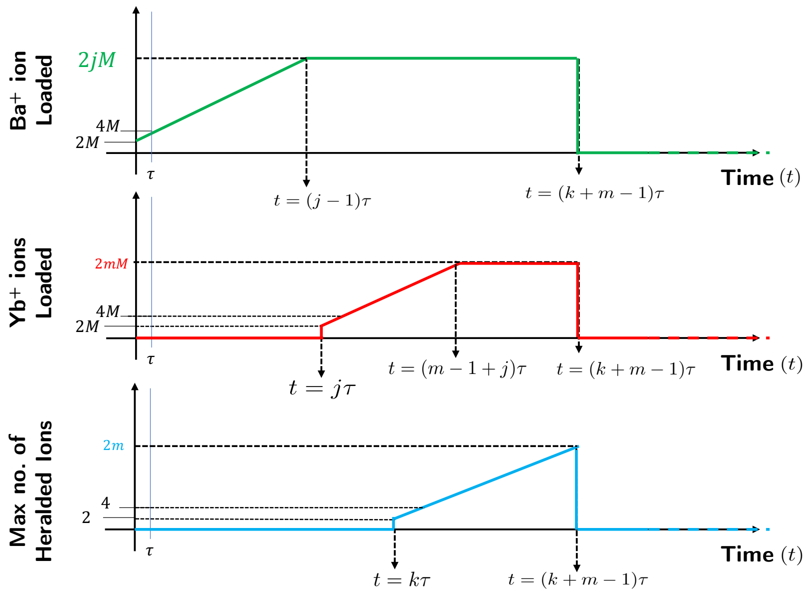

Figure 9. Timing diagram for Table I Type A Case 2

Case 2	Ba^+ Occupancy			Yb^+ Occupancy		Max. number of heralded ions
Time	Initialized	Freed	Loaded	Loaded	Freed	
0	$2M$	-	$2M$	-	-	-
τ	$4M$	-	$4M$	-	-	-
$\vdots$	$\vdots$	$\vdots$	$\vdots$	$\vdots$	$\vdots$	$\vdots$
$k\tau$	$2(k+1)M$	$2(M-1)$	$2(kM+1)$	-	-	-
$\vdots$	$\vdots$	$\vdots$	$\vdots$	$\vdots$	$\vdots$	$\vdots$
$(k+j)\tau$	$2(k+j+1)M$	$2(M-1)(j+1)+2$	$\mathbf{2(kM+j)}$	2	-	2
$\vdots$	$\vdots$	$\vdots$	$\vdots$	$\vdots$	$\vdots$	$\vdots$
$(\mathbf{k+j+m-1})\tau$	$2(k+j+m)M$	$2(M-1)(j+m)+2m$	$2(kM+j)$	$\mathbf{2m}$	$-$	$\mathbf{2m}$

Table VI. Timing chart for Tables IV B and C, Case 2, i.e., when $(\tau_o > k\tau > j\tau) \wedge (\tau_0 > (k+j)\tau > k\tau)$ and $(\tau_0 > j\tau > k\tau) \wedge (\tau_0 > (k+j)\tau > j\tau)$, respectively.The timing diagram for this protocol type is shown in Fig. 10.

Case 2	Ba^+ Occupancy			Yb^+ Occupancy		Max. number of heralded ions
Time	Initialized	Freed	Loaded	Loaded	Freed	
0	$2M$	-	-	-	-	-
τ	$4M$	-	-	-	-	-
$\vdots$	$\vdots$	$\vdots$	$\vdots$	$\vdots$	$\vdots$	$\vdots$
$k\tau$	$2(k+1)M$	-	-	-	-	-
$\vdots$	$\vdots$	$\vdots$	$\vdots$	$\vdots$	$\vdots$	$\vdots$
$j\tau$	$2(j+1)M$	$2M$	$\mathbf{2jM}$	$2M$	$2(M-1)$	2
$\vdots$	$\vdots$	$\vdots$	$\vdots$	$\vdots$	$\vdots$	$\vdots$
$(\mathbf{j+m-1})\tau$	$2(j+m)M$	$2mM$	$2jM$	$\mathbf{2mM}$	$2m(M-1)$	$\mathbf{2m}$

Table VII. Timing chart for Table IV C, Case 1, i.e., when $(\tau_0 > j\tau > k\tau) \wedge ((k+j)\tau > \tau_0 > j\tau)$. The timing diagram for this protocol type is shown in Fig. 11.

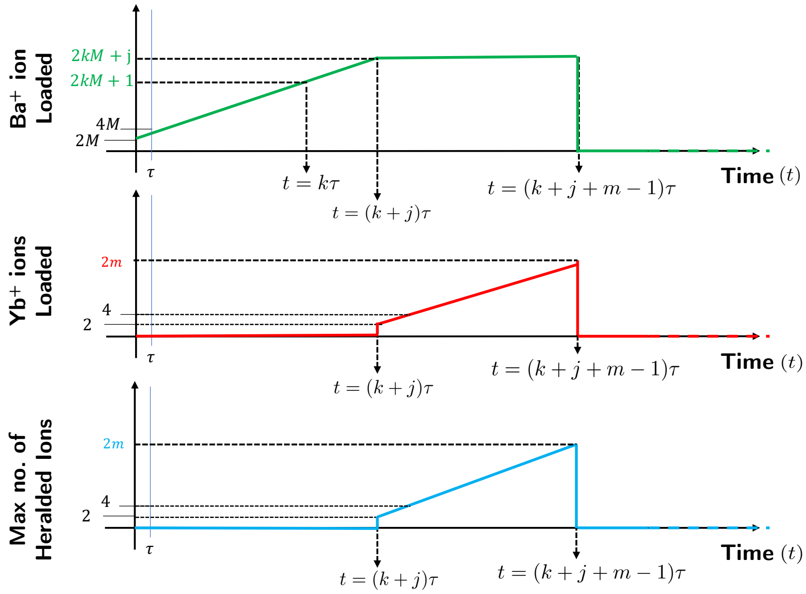

Figure 10. Timing diagram for Table I Type B

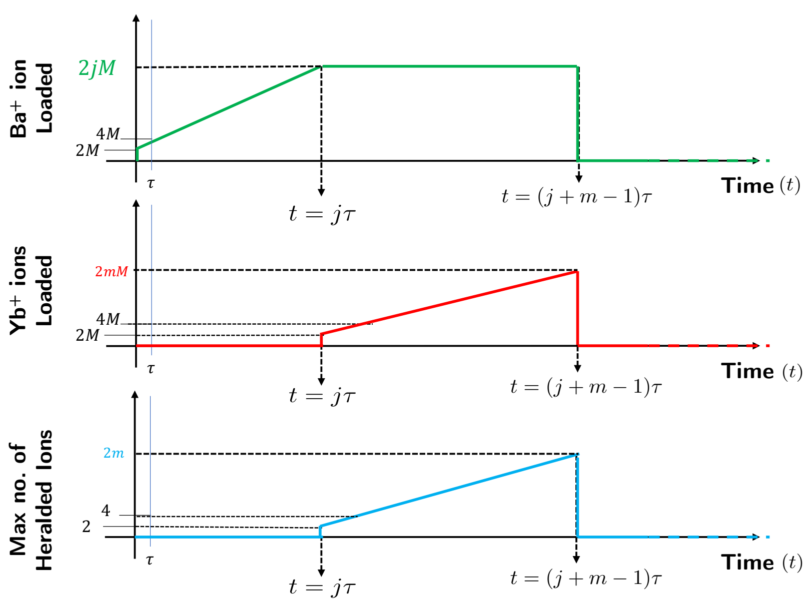

Figure 11. Timing diagram for Table I Type C

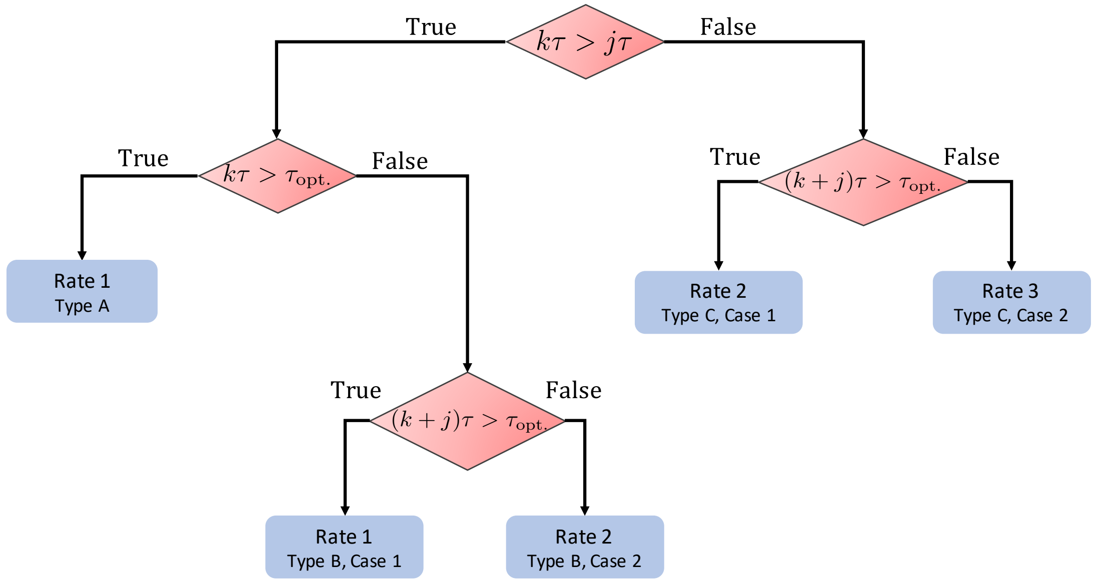

Figure 12. Decision tree to determine relative timing parameter ordering and associated rate equations.